PREPARED FOR THE U.S. DEPARTMENT OF ENERGY,
UNDER CONTRACT DE-AC02-76CH03073

PPPL-3792
UC-70

PPPL-3792

Chapter 6: NCSX Plasma Heating Methods

by

H.W. Kugel, D. Spong, R. Majeski, and M. Zarnstorff

February 2003

PPPL
PRINCETON PLASMA
PHYSICS LABORATORY

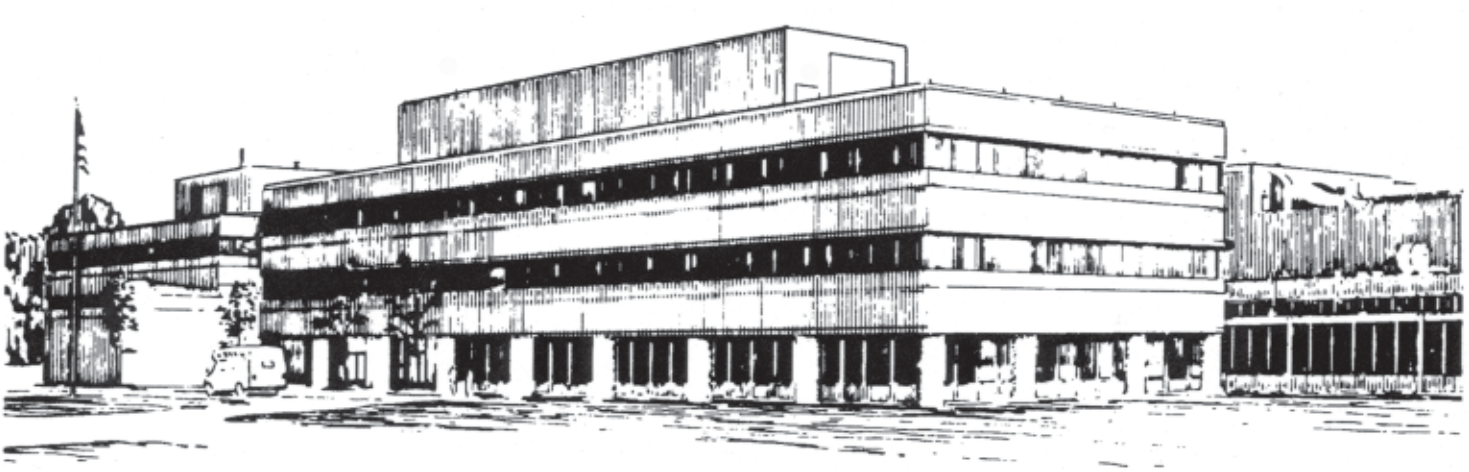

PRINCETON PLASMA PHYSICS LABORATORY
PRINCETON UNIVERSITY, PRINCETON, NEW JERSEY

PPPL Reports Disclaimer

Availability

This report is posted on the U.S. Department of Energy's Princeton Plasma Physics Laboratory Publications and Reports web site in Fiscal Year 2003. The home page for PPPL Reports and Publications is: http://www.pppl.gov/pub_report/

DOE and DOE Contractors can obtain copies of this report from:

U.S. Department of Energy
Office of Scientific and Technical Information
DOE Technical Information Services (DTIS)
P.O. Box 62
Oak Ridge, TN 37831

Telephone: (865) 576-8401

Fax: (865) 576-5728

Email: reports@adonis.osti.gov

This report is available to the general public from:

National Technical Information Service
U.S. Department of Commerce
5285 Port Royal Road
Springfield, VA 22161

Telephone: 1-800-553-6847 or
(703) 605-6000

Fax: (703) 321-8547

Internet: http://www.ntis.gov/ordering.htm

Chapter 6. NCSX Plasma Heating Methods

H.W. Kugel[1], D. Spong[2], R. Majeski[1], M. Zarnstorff[1]

[1] *Princeton Plasma Physics Laboratory, Princeton, NJ 08543, USA*

[2] *Oak Ridge National Laboratory, Oak Ridge TN, 37831, USA*

Abstract

NCSX has been designed to accommodate a variety of heating systems, including ohmic heating, neutral beam injection, and RF. Neutral beams will provide one of the primary heating methods for NCSX. In addition to plasma heating, neutral beams are also expected to provide a means for external control over the level of toroidal plasma rotation velocity and its profile. The experimental plan requires 3MW of 50 keV balanced neutral beam tangential injection with pulse lengths of 500 msec for initial experiments, and to be upgradeable to pulse lengths of 1.5 sec. Subsequent upgrades will add 3 MW of neutral beam injection. This Chapter discusses the NCSX NBI requirements and design issues, and shows how these are provided by the candidate PBX-M NBI system. In addition, estimations are given for beam heating efficiencies, scaling of heating efficiency with machine size and magnetic field level, parameter studies of the optimum beam injection tangency radius and toroidal injection location, and loss patterns of beam ions on the vacuum chamber wall to assist placement of wall armor and for minimizing the generation of impurities by the energetic beam ions. Finally, subsequent upgrades could add an additional 6 MW of RF heating by mode conversion ion Bernstein wave (MCIBW) heating, and if desired as possible future upgrades, the design also will accommodate high harmonic fast wave and electron cyclotron heating. The initial MCIBW heating technique and the design of the RF system lend themselves to current drive, so that if current drive became desirable for any reason only minor modifications to the heating system described here would be needed. The RF system will also be capable of localized ion heating (bulk or tail), and possibly IBW generated sheared flows.

6 Introduction

NCSX is designed to accommodate a variety of heating systems, including ohmic heating, neutral beam injection, and RF. The experimental plan requires ohmic heating and 3MW of balanced neutral beam injection for initial experiments, and to provide for subsequent upgrades that could add an additional 6 MW of ICRF and 3 MW of neutral beam injection.

6.1 Ohmic Heating

The ohmic heating capability will be implemented using the poloidal field coils, and provides inductive heating up to $\pm$420 kA of ohmic current. This will be used for initial breakdown and formation of target plasma for neutral beam heating. It will also be used to manipulate the current profile shape, allowing relatively rapid equilibration with the bootstrap current, as discussed below (refer to Chp. 9).

6.2 Neutral Beam Injection Heating

The NCSX design will use the PBX-M NBI system consisting of 4 beamlines with a total injection power of 6 MW, H^0 at 50 kV for 0.5 sec, or 8 MW, D^0 at 50 kV for 0.5 sec. The initial configuration will utilize two of the four existing PBX-M neutral beams; one aimed in the co-direction, and the other aimed in the counter-direction. The design will allow the other two beamlines be installed in a similar manner as a future upgrade. This Section gives a general overview of the NBI system characteristics and the configuration features required by the design.

6.2.1 Neutral Beam System Characteristics

6.2.1.1 Available Injection Power

NCSX NBI system will have one ion source per beamline. The ion sources have 30 cm circular copper grids and a focal length of 440 cm. Each ion source was fabricated, tested, and fully qualified at ORNL in 1979-1980 to power levels of 1.5 MW, H^0 (at 50 kV, 100A, 0.3 sec) for the PDX experiment.[1] In addition, one ion source was demonstrated to yield 2 MW, D^0 (at 50 kV, 70A, 0.3 sec). Subsequent testing after installation on PDX demonstrated the capability to inject 8.3 MW, D^0 with four sources in the absence of magnetic fields. The presence of stray magnetic fields and finite transition duct pressure reduced the available power to 6.5-7.0 MW, D^0. This loss of reionization power of 12-18% will be regained in NCSX by reinstalling, in the beamline exit region, the 100 kl/s cryopumping capability of the original ORNL design.

6.2.1.2 Neutral Species Ratios

NSCX neutral beam design requires high, full energy, injected neutral power fractions. The PBX-M NBI system meets this requirement. Typical species measurements performed at ORNL with equilibrium density neutralizer cells using ion dump yields found ion source species ratios of $H^0(E):H^0(E/2):H^0(E/3)$ = 63:20:17, and neutral beam power output ratios of $P^0(E):P^0(E/2):P^0(E/3)$ = 80:13:7. [1] On PDX, with D^0 at 47 keV, (1.6 MW), using Rutherford Backscatter Spectroscopy on the injected neutrals found neutral particle ratios of $D^0(E):D^0(E/2):D^0(E/3)$ = 53:32:15, and neutral power ratios of $P^0(E):P^0(E/2):P^0(E/3)$ = 72:21:7. [2]

6.2.1. 3 Pulse Length

The NCSX program plan calls for initial NBI heating pulse lengths of 300 msec, and then extending the heating pulse lengths to 500 msec. At a later experimental stage, the beamline hardware may be upgraded to accommodate 1.5-3 sec NBI pulse length capability. The original neutral beamline power handling surfaces were engineered to operate at a maximum of 500 msec pulse lengths at the full power peak power density of 3 kW/cm^2. In addition to power conditioning each of the ion sources at pulse lengths of 300 msec, ORNL in 1979-1980 demonstrated one ion source to operate at 500 msec pulse lengths using H^0 at about 50 kV, 90A. Similar results were obtained on PBX-M, with

modest changes, where each of the 4 neutral beamlines was demonstrated to operate with D^0 at ~40 kV, 1 MW , to pulse lengths of 500 msec.

6.2.1. 4 Control and Performance

The NCSX NBI design will use computer control to optimize NBI availability, and reliability. In the case of PDX, after NBI installation, the project developed full computerization for the NBI system, including control of filament, arc, and acceleration grid conditioning, and fault response using an "artificial intelligence" or "expert rules" algorithm.[3,4] One operator monitored all four systems in a “hands-off” manner. The computer control was found to provide unforeseen benefits in operational reliability, reproducibility, and safety. This software is available and will be ported to a new NCSX dedicated NBI computer system to facilitate operations.

6.2.1. 5 Ion Source Focal Length, Focusing, and Power Density Profiles

The required NCSX NBI power determines vessel access requirements, since the injected power depends on the effective focal length, focusing, and steering of the output neutral beam. These factors are significant considerations in the design of long, tight, transition ducts for tangentially injecting beams.

The PBX-M ion sources consist of 3 circular grids, 30 cm in diameter containing about 2000 circular holes for producing 2000 circular beamlets. The grids are shaped spherically concave to provide geometric focusing (aiming) with a focal length of 440 cm, which was the distance to the PDX torus port (Figure 6-1). The NCSX NBI alignment will place this focal plane in the narrowest region of the transition duct.

The required grid curvature was modeled using a gaussian geometric optics code.[5] Measurements of the respective as-built focal lengths and focusing were performed using a pinhole camera technique and power density profile measurements at the focal plane torus target.[1] The final measured focal lengths were consistent with the

design value of 440 cm. Table 6-1 gives the H^o angular divergences for each neutral beam at the torus target horizontal focal plane (440 cm). The results shown in Table 6-1 were obtained from measurements of the respective beam power density profiles measured along the horizontal axis in the focal plane at the torus target using a scanning water calorimeter behind pin-hole apertures (Figure 6-2). The results exhibit a gaussianbehavior from peak power density down to about 10% of peak power density. Below the 10% power level, the profiles exhibit "wings" that have been characterized by asymmetric Gaussian, or polynomial least-squares fitting.

The NCSX neutral beam configurations and transition duct designs use the above results. The solid and dashed lines in Figure 6-3 show the simulated beam power density profile along the beam axis using a gaussian geometric optics fit to the measurements given in Table 6-1. These power density profiles were used to achieve a duct design that meets the NCSX injected NBI power requirements.

6.2.1. 6 Maximizing Absorbed Power

The NSCX transition duct design, although sufficiently large to accommodate the above power density profiles, also helps to reduce system gas pressure (from the ion source and neutralizer gas flow) in the transition region which causes reionization, and loss of neutral particles. The subsequent deflection of reionized beam particles into the duct walls by the fringe magnetic field causes additional gas load from out-gassing and an avalanching of reionized power loss (~2-20%, depending on path length and pressure). Maintaining NCSC NBI transition region neutral gas pressure in about the 10^{-5} torr regime will significantly increase injected power. The NCSX design will accomplish this by optimizing the duct design and by installing additional cryopumping in the front box of the beamline. Table 6-2 shows the NBI system injected power capability and the effects of fringe fields for PBX-M.

6.2.1. 7 Maximizing Desired Neutral Beam Species

The NCSX NBI design goal of maximizing the available NBI power requires maximizing the full energy particle component available from the available ion sources. Typically, the PBX-M neutral beamlines were operated with the neutralizer cell at ~90-95% equilibrium gas pressure to optimize the yield of the full energy component. Sec. 6.2.1.2 above discusses the measured NBI system neutral species yields. NBI system gas from the ion source and neutralizer in the transition duct can change the fractional ionic yield of the low energy components and produce small differences in the species ratios of injected beam.[2] The NCSX design will install additional cryopumping in the front box of the beamline to reduce this effect.

6.2.1. 8 Power Transmission to the Far-Wall

The NCSX NBI design includes far wall armor to provide vessel wall safety without relying entirely on interlocks. Neutral beam power transmission to the far-wall of the vessel ("shine-through") requires at minimum sufficient armor to absorb a short full power pulse. In PBX-M, this armor was designed to absorb at least a short full power pulse so as to allow power and position calibration injections in the absence of plasma. Sometimes in PBX-M, this armor was used to absorb short neutral beam conditioning pulses if the beamline calorimeter was unavailable. Similarly for NCSX, rather than rely completely on either thin armor or no armor, plus interlocks to stop beam injection beyond an acceptable pulse length, the NCSX plan is to achieve a beam armor design capable of stopping a full power, 0.5 sec, beam injection in the absence of plasma (*e.g.*, 1.3 cm thick graphite is an acceptable armor for a 3 kW/cm^2 power deposition for 0.5 sec).

Figure 6-4 shows a plot of the estimated transmission through PDX plasmas *versus* density for H^0 and D^0 at 40 and 50 keV. These results indicate that, for example, ATJ graphite at least 1.3 cm thick or the equivalent will be sufficient for wall armor tiles capable of absorbing the available peak NBI power densities of 3 kW/cm^2 for 500 msec in the absence of plasma. Thicker tiles with active cooler would be needed as an upgrade

for longer NBI pulse lengths if full power, full pulse length capability are desired for additional vessel safety. The NCSX NBI plan is to install uncooled, wall armor tiles, at least 1.3 cm thick, prior to first injection. The actual design will await the completion of other in-vessel hardware.

6.2.1. 9 Minimizing Duct Wall Conditioning

The NCSX NBI design will minimize the time required for transition duct wall conditioning. This procedure is often practiced by high powered NBI systems using short, low power pulses prior to the start of high power injection operations. Gas absorbed on and in duct walls during non operating periods and during operations is released (outgasses) under this particle bombardment and heating. The reduction of strong initial duct outgassing is desirable to prevent "duct choking" *i.e.,* dangerous reionized power losses. In addition, reduction of daily duct outgassing results in increased injected power, and provides more reproducible results. Figure 6-5 shows the measured PDX East NBI system duct outgassing *versus* the cumulative power absorbed over several months. It is seen that, initially at the beginning of a 1-2 week experimental campaign, the duct outgassing was high but decreased steadily during the experimental campaign. Interruption of the campaign for maintenance resulted in the return of high outgassing rates due to fresh gas absorbed on the duct walls from the vessel, and volume diffusion of fresh gas to the surface of the duct walls to replenish the outgassed surface region. The NCSX NBI design will reduce duct outgassing by using high conductance geometry, with walls far from the beam, appropriate materials, baking, and HeGDC between discharges The NCSX design will include the installation of high-speed cryopumping, in the exit box of the beamlines, at the entrance to the duct, to significantly reduce or eliminate the effects of residual duct outgassing. This hardware will also accelerate NCSX pumpdown between discharges.

6.3 Fast Ion Confinement Analysis for NCSX

6.3.1 Introduction

Neutral beams will provide one of the primary heating methods for NCSX; up to 6 Mw of beam power will be available in the 40 to 50 keV energy range. These beams will be injected tangentially in both the co- and counter- directions in order to minimize beam driven currents. In addition to plasma heating, beams are also expected to provide a means for external control over the level of toroidal plasma rotation velocity and its profile.

NCSX has been designed to be as toroidally symmetric as possible in magnetic Boozer coordinates.[6] This leads to improved energetic beam ion confinement and higher predicted heating efficiencies in comparison to more conventional stellarators. However, even in such an optimized stellarator, there will remain some non-zero departure from perfect symmetry. These deviations will lead to somewhat enhanced levels of beam ion losses above those present in an equivalent symmetric tokamak. For example, localized magnetic wells in the stellarator can result in small fractions of locally trapped orbits that drift directly out of the plasma; this ripple can additionally cause banana orbits trapped in the 1/R wells to gradually leave the plasma due to the successive perturbations in their bounce points. Barely passing particle orbits are also perturbed by low levels of this ripple; their orbits can become stochastic over many toroidal transits and leave the plasma.

The above orbital effects require careful analysis for neutral beam heating since they are especially exacerbated by the nearly collisionless nature and high transit speed of the beam ions. This forms the motivation for the following set of calculations. The model described below is used for estimations of beam heating efficiencies (important for plasma performance estimations), scaling of heating efficiency with machine size and magnetic field level, parameter studies of the optimum beam injection tangency radius and toroidal injection location, and loss patterns of beam ions on the vacuum chamber wall (important for placement of wall armor and for minimizing the generation of impurities by the energetic beam ions).

6.3.2 Description of Model

Our model (the DELTA5D code [7]) is based on the geometry shown in Figure 6-6. A diffuse beam is injected into the plasma on the equatorial plane ($\theta = 0$) at a particular toroidal angle $\zeta_{inj.}$. The deposition profile for the beam is externally specified and is obtained from the modeling of similar axisymmetric systems (using the cross-sectional shape at the $\zeta = \pi/3$ plane) using TRANSP [8]. Particles are initially distributed over flux surface locations in consistency with this deposition profile. In order to determine the initial pitch angle distribution for the beam, a pencil beam model is used. For each beam particle (at flux surface ψ, $\theta = 0$, $\zeta = \zeta_{inj}$) we calculate it's major radius, R; initial pitch angles are then determined by the pencil beam relation: $v_{||}/v = R_{tan}/R$. Only flux surfaces having major radii (at $\theta = 0$) > R_{tan} are populated with beam ions. The expectation is that as the beam ions slow down and pitch angle scatter they will lose "memory" of their initial conditions in pitch angle, θ, and ζ and thus not be too sensitive to the model used for these coordinates. Since their losses will be more sensitive to their initial flux surface locations, our model allow that to be determined independently, using a specified diffuse beam deposition profile.

From these initial conditions, the beam particle orbits are then followed by solving Hamiltonian guiding center equations which time advance the particles in the two angular coordinates (poloidal and toroidal angles in Boozer coordinates) and the conjugate momenta. Equilibrium magnetic fields are obtained from the VMEC stellarator equilibrium code [9] which are then transformed to Boozer coordinates.[6] Collisions with a static background plasma consisting of electrons and two background ion species (a main ion and one impurity component) are simulated using a Monte Carlo collision operator [10] based on pitch angle and energy scattering terms, taking into account the full velocity-dependent potentials [11] without assumptions regarding relative orderings of the electron, beam ion and impurity velocities. Collisions are allocated on a fixed time step Δt_{coll} which is chosen so as to maintain $\nu\Delta t_{coll} << 1$ and to allow a smooth granularity in modeling the collisional processes. The time integration step for the orbit integration is controlled by the ordinary differential equation solver LSODE [12] which internally choses an integration time step so as to maintain a

prescribed accuracy level. The typical variation of the different beam ion collision frequencies with velocity and flux surface included in this model are shown, respectively, in Figures 6-7(a) and 6-7(b).

The subscripts on the collision frequencies denote the species (electrons, ions, impurities) which the beam is colliding with and whether the collision frequency pertains to pitch angle deflection (D) or energy scattering (E). Currently we do not include collisions with neutrals. Typically, the beam ions are injected at a velocity where they are slowing down somewhat more on electrons than ions, but they soon pass through the critical energy, below which they begin slowing down more on ions. Also as the beam ions pass through the critical energy, pitch angle scattering begins increasing; this can result in higher fast ion losses as the ions get scattered out of the passing region of velocity space. As the beam ions slow down to 3/2 kT_{ion} (with T_{ion} being the background field ion temperature), they are counted as part of the background plasma species. Beam ions that pass through the outer flux surface are removed from the distribution and not replaced; thus, the quoted loss rates may be a slight overestimate. Beam heating efficiencies are calculated by recording the losses of particles and energy out of the outer magnetic flux surface that occur during the slowing-down process. The DELTA5D code[7] follows groups of beam particles on different processors in parallel using the MPI language for inter-processor communication. It has been adapted to both the Cray T3E and IBM-SP computers. A variety of diagnostics of the escaping particles, such as pitch angle, energy and particle lifetime distributions, are retained to aid in understanding the loss mechanisms.

In Figures 6-8(a) and 6-8(b) we show some of the characteristics of a slowing-down beam for the parameters $n(0) = 8 \times 10^{19}$ m^{-3}, $T_e(0) = 2.9$ keV, and $T_I(0) = 2.0$ keV. Figure 6-8(a) shows on the left-hand scale the time evolution of the percentage of energy lost from the beam averaged over the ensemble of 2,048 particles used here. We normally follow the distribution of beam particles until this energy loss fraction reaches a saturated plateau; this flattening is associated with the average beam ion slowing down to the 3/2 kT_{ion} energy level [shown on the right-hand scale in Figure 6-8(b)]. Figure 6-8(a)

also shows the time variation of the ensemble averaged ratio of magnetic moment to energy for the beam. Initially this ratio starts out small due to the anisotropic nature of the beam (i.e., composed mostly of passing orbits) and then increases as the beam pitch angle scatters and spreads out to become more isotropic. Finally, Figure 6-8(b) shows the decrease in time of the number of beam particles, indicating the degree to which particles are lost at times prior to that required for slowing down enough to join the background distribution.

Figures 6-9(a) and 6-9(b) show histograms of the energy and pitch angle distributions of the escaping beam ions for the case shown in Figure 6-8. As can be seen, the energy losses are characterized by a broad peak centered around 15 - 20 keV for both co- and counter- injection. The counter-injected ions also show a very sharp peak at the injection energy, presumably associated with prompt losses.

The pitch angle distributions of escaping ions shown in Figure 6-9(b) are mostly peaked around the deeply trapped range of pitch angles with a secondary peak (for the co-injected ions) more in the transitional region. The counter-injected ions show a very sharp peak near $v_{||}/v = 0.7 - 0.8$ which is close to the birth pitch angle, indicating a prompt loss component for the case of a tangency radius $R_{tan} = 1.38$ m.

6.3.3 Parameter Scans

We have used the model described above to study sensitivity to variations in configuration, beam and plasma parameters. In Figures 6-10 and 6-11, we have used the NCSX,[13] m45 configuration, with a volume averaged magnetic field of 1.6 Tesla, and an average major radius of 1.4 meters. The central plasma density is nominally 8×10^{19} m^{-3} and the central ion temperature was 2 keV and the electron temperature was 2.9 keV; the plasma species is hydrogen. An impurity species is present with Z = 18, A = 9, at 1% of the electron density, and a temperature equal to the background ion temperature. The beam is also taken as hydrogen and is monoenergetic at injection with an energy of 40 keV. The beam is initially deposited at $\theta_{inj} = 0$, $\zeta_{inj} = \pi/3$. Plasma profiles for temperature

and density have been determined from 1-D transport modeling and the ambipolar potential is set to zero.

In Figure 6-10 the tangency radius for injection is varied. As the tangency radius is made smaller, the beams are initially launched onto larger pitch angles relative to the magnetic field (smaller $v_{||}/v$). This puts them closer to the trapped-passing transitional regime of velocity space where orbits are more likely to experience prompt losses. As may be seen, the losses steadily increase for both co- and counter injected ions as R_{tan} is decreased. The minimum for the counter-injected curve is close to the point where R_{tan} = the magnetic axis location. For this configuration the magnetic axis at the toroidal injection angle ($\zeta_{inj} = \pi/3$) was 1.38 m. As R_{tan} is increased beyond this point, the counter-injected losses again increase due to the fact that the beam ions are progressively being aimed further out in minor radius leading to hollow deposition profiles and increased fractions of prompt orbit losses. The co-injected losses continue to decrease as R_{tan} is increased beyond the magnetic axis location. This results for several reasons. First, as R_{tan} is increased the pitch angle distribution of the beam becomes increasingly aligned with the magnetic field (i.e, near $v_{||}/v = 1$) and thus further from the lossy trapped-passing region. Also, the beam distribution becomes more localized to the plasma edge; for the profiles of temperature and density used here, the slowing-down time is shorter near the edge. More rapid slowing-down results in lower losses for the beam ions since they spend less time at high energies where losses are larger. Finally, for co-injected beams the prompt losses are low so that the nearness of the beam to the plasma edge does not enhance losses to the extent that it does for counter-injected beams. The main issue that needs to be resolved as R_{tan} is increased for co-injected beams is how this affects the heating deposition profile. At some point this may become too hollow to be of interest.

In Figure 6-11 we examine the variation of beam losses as the magnetic field is changed, using 40 keV beams. As may be seen, there is a monotonic decrease in beam losses with increasing magnetic field strength with counter-injected losses being larger

than co-injected losses. Figures 6-12 and 6-13 show the pitch angle and energy spectra of the escaping beam ions as the magnetic field strength is varied.

As indicated in Figure 6-9(a), a large fraction of the escaping beam ions leave the plasma with 1/3 to 1/2 of their initial injection energy. It is desirable to intercept this power deposition on the vacuum chamber wall by localized protective armor plating to minimize impurity generation and wall erosion. In order to design such structures, it is necessary to make estimates of the wall locations where the escaping beam ions will be deposited. As a first step toward such estimates, as the beam ions leave the outermost closed flux surface, we record their exit locations, exit times, pitch angles and energies. It should be noted that these are only the loadings at the outer flux surface and may not reflect the distributions of lost ions at the vacuum chamber wall. More realistic models will need to be developed which follow the fast ion trajectories in the outer region where flux surfaces no longer exist. Results at the outermost flux surface based upon the current model are shown in Figure 6-14 and 6-15 for a typical case. Here the exit locations are plotted in Boozer poloidal and toroidal angle coordinates. These losses are superimposed on contours of |B| and magnetic field lines. The fast ion losses are primarily concentrated in helical stripes following the field lines on the bottom of the stellarator with one stripe per field period. In the case of counter-injected beams there are also some losses (possibly prompt) near the inboard region of the torus ($\theta \sim \pi$).

Finally, we have plotted the ion loss locations on the three-dimensional outermost flux surface (Figure 6-16) as obtained from the VMEC stellarator equilibrium code. The flux surface is shown in red and the ion exit locations are color coded according to the ion's energy at the time it passes through the flux surface. Exit positions for both co- and counter-injected beam ions are indicated. Again, it can be seen that the losses are somewhat concentrated, motivating the design of protective structures at these locations. These issues will be further discussed in Chapter 10.

6.3.4 Suggestions for Future Work

The model described here has been developed for comparative studies of different NCSX configurations and to obtain approximate estimates of beam heating efficiencies and loss patterns. In order to develop an adequate physics understanding of fast ion confinement in a real experiment, a number of upgrades and new tools will need to be developed. Although many of these issues have already been thoroughly examined for tokamaks, the inherently 3D nature of the stellarator geometry will, in many cases, require a complete re-development of existing tools.

In the area of neutral beam deposition, finite width, multiple energy group beam models will need to be developed and their intersection with the 3D flux surface shapes taken into account. As the beam ions slow down, collisions with neutrals and multiple impurity species should be modeled; beam-beam self collisions and finite beam gyroradius effects may also be of relevance for some regimes. A number of additional physics diagnostics for beam ion effects can readily be included in the Monte Carlo calculations. For example, beam-driven currents and transfer rates of beam energy to the different plasma species can be obtained. Other diagnostics, such as predictions of the energy distributions of charge exchange neutrals escaping the plasma, can be useful in interpreting charge exchange measurements.

The beam slowing down model described here assumes nested, closed flux surfaces. Stellarators can develop magnetic islands and open field lines at some point near the plasma edge. In determining beam loss rates through these regions as well as beam loss patterns and heat loads on walls and divertors, it could be important to follow beam ion orbits into these regions by matching together Hamiltonian orbit models for the inner closed surface region with more conventional real space guiding center drift models for the regions outside the last closed flux surface.

6.4 Radio Frequency Heating

6.4.1 Introduction

The radio frequency (RF) heating system for NCSX will be designed to deliver 6 MW of radio frequency (RF) power to the plasma. The primary requirement is for electron heating, since the NBI system is expected to provide ion heating. At present there is no projected need for current drive capability in order to cancel residual currents driven by neutral-beam injection during unbalanced injection, or to further tailor the equilibrium. However, the chosen RF heating technique and the design of the RF system lend themselves to current drive, so that if current drive became desirable for any reason only minor modifications to the heating system described here would be needed. The RF system will also be capable of localized ion heating (bulk or tail), and possibly IBW generated sheared flows.

The RF heating technique chosen for NCSX is mode conversion ion Bernstein wave (MCIBW) heating. NCSX is designed to accommodate high harmonic fast wave and electron cyclotron heating as possible future upgrades. However, such systems are not planned at this time.

6.5 Mode Conversion RF Heating

6.5.1 Introduction

In mode conversion ion Bernstein wave heating, a fast magnetosonic wave, excited at the boundary of a multiple-ion species plasma, propagates to the ion-ion hybrid layer where it undergoes conversion to the slow wave. Typically, the damping lengths for the slow ion Bernstein wave (IBW) are many times shorter than for the launched fast wave, so that power deposition occurs in a highly localized region near the hybrid layer. When the ion temperature is modest and the species mix is such that mode conversion takes place far from an ion cyclotron resonance, the IBW damps on electrons. For high

ion temperatures, or modest concentration of one of the ion species so that the mode conversion layer is located close to a cyclotron resonance, ion damping can be produced.

Mode conversion heating was first successfully demonstrated using a high field side launch in the TFR tokamak.[14] Efficient, localized electron heating using mode conversion was predicted [15] and demonstrated [16] in TFTR, and more recently has been extensively utilized in C-MOD.[17] In tokamaks, a low field side launch of the fast wave in D-^{3}He has been most commonly employed. The choice of a low field side launch is primarily by available hardware, and the difficulties inherent in siting antennas on the high field side of a tokamak. Mode conversion with a high field side launch, which is very efficient with a wider variety of ion species mixes, has now been utilized successfully in the LHD [18], WVII-AS [19], and CHS [20] stellarators. Modeling of NCSX plasmas has indicated that a high field side fast wave launch is necessary to efficiently access the mode conversion regime. Although such a launch would have been exceedingly difficult or impossible to accommodate with the original saddle-coil design for NCSX, the modular coil design will permit installation of a high field side antenna. The antenna will be constructed with a relatively small radial build, which lends itself to installation in a shallow "pocket" in the vacuum vessel, on the high field side.

The METS 95 code, a 1-D hot plasma full-wave code which has been extensively benchmarked during mode conversion heating experiments in TFTR and C-MOD, has been employed to model mode conversion in NCSX. Mode conversion scenarios for NCSX have now been identified for D-H and D-^{3}He plasmas. Either ion or electron heating can be selected through an appropriate choice of the species mix and launched wavenumber.

6.5.2 Mode Conversion in D-H

The results of modeling D-H mode conversion are shown in Figure 6-17 (a & b). Figure 6-17(a) is a plot of the dispersion relation for 10% H in a D majority plasma, with a central magnetic field of 1.6T, a central electron density of 5×10^{19} m^{-3} (parabolic

profile), for a fast wave excited at 20 MHz with a wavenumber of 9 m^{-1}. Ionic species concentrations are given as (n_{ion}/n_e). Note that this and all following modeling is largely invariant in (ω/Ω_i); if operation at a lower (higher) magnetic field is desired then the launch frequency must be reduced (increased).

For the ion and electron temperatures chosen (T_e=T_i= 1 keV), METS 95 indicates that majority D/minority H mode conversion will produce relatively weak absorption, with a broad deposition profile on the electron population. Since absorption occurs well to the high field side of the hydrogen cyclotron resonance, a relatively high magnetic field is required to obtain core heating with this mode conversion scenario.

Although the option to use hydrogenic plasmas would permit access to possible low-recycling regimes, operation at the lower toroidal field initially available on NCSX with core heating would require a prohibitively low operating frequency (~15 MHz). Finally, lower hydrogen concentrations (~5%) would allow experiments in conventional light ion minority heating, although the fast ion tail population may not to be well confined in NCSX.

6.5.3 Mode Conversion in H-^{3}He

The most promising and flexible ion system for mode conversion heating in NCSX is H-^{3}He, which should permit localized ion or electron heating (or electron current drive), either on or off axis. With a transmitter frequency of 20 MHz (the lowest practical frequency for the existing PPPL sources), on axis heating can be obtained at central magnetic fields as low as 1.3T.

Localized electron heating can be produced in H-^{3}He for a wide range of species mixes and wavenumbers. In Figure 6-18(a) we display a dispersion relation computed for NCSX with 25% ^{3}He in hydrogen, for 20 MHz excitation at 1.5T central magnetic field. The dispersion relation for the IBW indicates that $k_\perp$ increases rapidly as the wave propagates away from the ion-ion hybrid layer, back towards the high field side.

Localized electron damping results, as shown in Figure 6-18(b). However, ion heating is predicted for low concentrations of either hydrogen (light ion minority) or helium (heavy ion minority). In Figure 6-19(a & b) the dispersion relation and deposition profile for 10% ^{3}He in H are shown. Deposition is predicted to be primarily on the helium-3 population. In order to produce ion heating it is necessary to launch the fast wave at high wavenumber (12 m^{-1}) to obtain Doppler-broadened Bernstein wave damping on the helium. In this case generation of an ion tail is not likely, since a larger (10%) minority ion population is heated, and since ^{3}He tail formation requires higher power densities and smaller minority populations than hydrogen minority heating.

Since the fast wave is mode converted to an IBW which subsequently damps on ions at the cyclotron resonance, it may be possible to generate sheared flow [21] with this heating technique. Note that if deposition at the 2/3 radius is desired (in order to increase the core plasma volume bounded by the shear flow layer), then the magnetic field can be reduced to 1.5T. Note also that the deposition layer (at least in this 1-D model) is extremely narrow, with a FWHM of only about 1 cm.

These capabilities (localized or broad electron heating, localized current drive or current profile control, localized ion heating, possible rf shear flow drive) combine to make mode conversion heating an attractive physics tool for NCSX.

6.6 RF Systems and Antennas for Mode Conversion

6.6.1 RF Systems

The existing PPPL FMIT units could be used for mode conversion heating in NCSX, in a time-sharing arrangement with NSTX. An engineering study has determined that operation of two of the four FMIT sources over the frequency range of 20 - 30 MHz is feasible; this would provide 4 MW of rf source power. An additional 3-4 MW would be available from the remaining two sources, depending on the degree to which they were

reconfigured. Although the sharing of sources precludes simultaneous RF heating of NSTX and NCSX, the transmitter modifications proposed would require minimal down time to change frequencies. A changeover from the NSTX operating frequency of 30 MHz to one of the NCSX operating frequencies (or the reverse) is expected to take a few days.

6.6.2 Antennas

The vacuum vessel design will accommodate three six-strap antennas, with each antenna installed in a recess in the vacuum vessel on the high field side. The depth of the recess varies from 9 to 16 cm deep, with a toroidal extent of 90 cm, and a poloidal extent of 37 cm. Each antenna is required to couple 2 MW of RF power, so the design power density at the antenna face is approximately 600W/cm^2, which is in the range of the JET and NSTX experiments. Each of the six straps will be fed through 4" coax. Accommodation for the 4" feedlines has been made in the vacuum vessel design (see Figure 6-20 a and b).The straps will be driven single ended (grounded at one end), and the Faraday shields and straps will be conformal to the plasma boundary.

The external matching system has not yet been designed. At the present time an externally coupled combline system is favored. Further modeling will be required to design a combline system which is tunable over the 20 – 30 MHz frequency range.

Although the final antenna design will incorporate six straps, initial installation of two straps at a single antenna location is planned in order to assess coupling and matching circuit requirements. Initial operation will utilize very low power sources for coupling studies in a later phase of NCSX. A short pulse transmitter with 500 kW output is available on-site for initial experiments. With a 500 kW source the power coupled per strap (250 kW) will be comparable to the design value (330 kW).

Acknowledgments

This work is supported by U. S. DoE Contracts DE-AC02-76CH03073 and DE-AC05-00OR22725.

References

[1] W. L. Gardner *et al*., Proc. of the 8th Symp. on Engineering Problems of Fusion Research, (November 13-16, 1979) 972.

[2] H.W. Kugel *et al*., Rev. Sci. Instrum. 56 (1985)1105.

[3] T. A. Kozub, *et al*., Proc. 12th Symp. on Fus. Eng. Res., (Monterey, CA, October 1987) 606.

[4] K. Tuttle-Frank, *et al*., Ibid. 596.

[5] J. Kim and J. Whealton, Nucl. Instrum. Methods. 141 (1977) 187.

[6] A.H. Boozer, Phys. Fluids **24** (1981) 1999.

[7] D.A. Spong, J. Carlsson, D.B. Batchelor, et al., Bull. Am. Phys. Soc. **44** (1999) 215.

[8] R.V. Budny, D.C. McCune, M.H. Redi, J. Schivell, R.M. Wieland, Phys. Plasmas **3** (1996) 4583.

[9] S.P. Hirshman, J.C. Whitson, Phys. Fluids **26** (1983) 3553.

[10] A.H. Boozer, G. Kuo-Petravic, Phys. Fluids **24** (1981) 851.

[11] S.P. Hirshman, D.J. Sigmar, Phys. Fluids **19** (1976) 1532.

[12] A.C. Hindmarsh, "Odepack, a Systematized Collection of ODE Solvers, in Scientific Computing," R.S. Stepleman et al. (Eds.), North-Holland, Amsterdam, 1983, pp. 55-64.

[13] M. Zarnstorff, 2000 IAEA Fusion Energy Meeting, Sorrento, Italy (Oct. 2000).

[14] Equippe TFR, in Plasma Physics and Controlled Nuclear Fusion Research, Proc. 9th International Conf., Baltimore, 1982, Vol. 2, p. 17.

[15] R. Majeski et al., Phys. Rev. Lett. **73** (1994) 2204.

[16] R. Majeski et al., Phys. Rev. Lett. **76** (1996) 764.

[17] P. T. Bonoli et al., Phys. Plasmas **7** (2000) 1886.

[18] T. Watari et al., Nucl. Fusion **41** (2001) 325.

[19] D. A. Hartmann, G. Cattenei et al., Fusion Energy 1998, C&S Papers Series 1/p (IAEA, Vienna, 1999) vol. 2, p. 575.

[20] S. Masuda et al., Nuclear Fusion **37** (1997) 53.[21] J. R. Wilson et al., Phys. Plasmas **5** (1998) 1721.

NBI System [a]	$\theta_{HW@HM}$ [b]	$W_{HW@HM}$ [c]	$\theta_{HW@1/e}$ [d]	$W_{HW@1/e}$ [e]
S	1.5°	11.58 cm	1.8°	13.9 cm
E	1.13°	8.75 cm	1.36°	10.5 cm
NW	1.2°	9.25 cm	1.44°	11.1 cm
SW	0.94°	7.25 cm	1.13°	8.7 cm

Table 6-1. Summary of NBI optics.

a) NBI System listed in order of ion source fabrication and testing at ORNL.

b) Angular divergence from centerline to edge at one-half of full power.

c) Beam half-width from centerline to edge at one-half of full power..

d) Angular divergence from centerline to edge at 1/e of full power.

e) Beam half-width from centerline to edge at 1/e of full power.

• **PBX-M Injected Power Capability** • **ORNL Qualification (No Fields)** $H^0 \rightarrow$ = 6 MW (4 x 1.5 MW) $D^0 \rightarrow$ = 8 MW (4 x 2.0 MW) • **PDX Testing (No Fields)** $D^0 \rightarrow$ 8.3 MW (4 NBI @ > 52 kV)
• **Neutral Power Reionization Loss Fractions in PBX-M Due to Duct Neutral Gas (~1-4x10^{-4} T)** • Perpendicular ducts $\rightarrow$ 0.88 P_0 (12% loss) • Tangential ducts $\rightarrow$ 0.83P_0 (17% loss)

Table 6-2. NBI power capability and reionization losses.

Figure Captions

Figure 6-1. Schematic diagram of PBX-M ion source grid optics. The ion source grids are curved so as to focus 2000 Gaussian beamlets at a focal point 440 cm from the grids. Ion source optics determine the duct size and achievable aiming angles.

Figure 6-2. Power density profile measured at ORNL for PDX ion source No.2 (East NBI). It was found that the resultant beam trajectory at the torus target at the exit of the transition duct is not accurately determined by simple, *apriori* mechanical alignment of the ion source, and that measuring the actual beam position in the duct is important for proper beam alignment.

Figure 6-3. Simulated power density along beam axis. The beam port location will allow adequate duct width to avoid neutral and reionized power impingement on the duct walls.

Figure 6-4. Plot of Neutral Beam power fractional transmission through a 90 cm thick PDX plasma *versus* density. This corresponds to the case of near-perpendicular injection (RTAN = 35 cm).

Figure 6-5. Measured PDX NBI duct outgassing during several months of operation (H.W. Kugel, et al., J. Vac. Sci. Technol., 20,(4) 1197 1982). H_2 Glow Discharge Cleaning (GDC) was used to clean the vessel immediately after pump-down from a vent. No H_2GDC or other GDC was applied thereafter. The application of HeGDC in the transition duct prior to NCSX daily operations and between discharges will reduce duct conditioning time significantly.

Figure 6-6. Geometry used for NCSX neutral beam calculations.

Figure 6-7(a). Collision frequencies vs. energy at r/a = 0.5 (collision frequencies with D/E subscripts denote pitch angle/energy scattering rates, respectively; ion, elect, imp subscripts denote beam collisions with plasmas ions, electrons, and impurities).

Figure 6-7(b). Collision frequencies vs. flux surface at E = 40 keV (collision frequencies with D/E subscripts denote pitch angle/energy scattering rates, respectively; ion, elect, imp subscripts denote beam collisions with plasmas ions, electrons, and impurities).

Figure 6-8(a). Typical evolution of ensemble averaged beam energy loss and $<\mu/\varepsilon>$; (b). Decay in time of the number of confined beam particles and average energy per particle.

Figure 6-9(a). Energy spectrum of exiting beam particles; (b). Pitch angle spectrum of exiting beam particles.

Figure 6-10 Dependence of beam losses on beam tangency radius for a version of NCSX with R_0 = 1.4 m.

Figure 6-11. Variation of beam losses with magnetic field for 40 keV hydrogen ions for a device with R_0 = 1.4 meters.

Figure 6-12. (a) Pitch angle spectrum of counter-injected losses as magnetic field is varied, and (b) Pitch angle spectrum of co-injected losses as magnetic field is varied.

Figure 6-13. (a) Energy spectrum of counter-injected losses as magnetic field is varied, and (b) Energy spectrum of co-injected losses as magnetic field is varied.

Figure 6-14. Location of co-injected beam losses (red dots) on outer surface in 2D Boozer coordinates with |B| contours and magnetic field lines (in red) shown.

Figure 6-15. Location of counter-injected beam losses (red dots) on outer surface in 2D Boozer coordinates with |B| contours and magnetic field lines (in red) shown.

Figure 6-16. Location and energy spectrum of co- and counter-beam losses on outer surface in 3D (the outer flux surface is shown in red).

Figure 6-17. Dispersion relation for mode conversion in 10% H/90% D in NCSX (a), and power deposition profile (b). 82% of the launched power is deposited on electrons within the simulation window, with a full-width at half-max of ~15 cm. Central density for the simulation was 5×10^{19} m^{-3} (parabolic profile), central $T_e = T_i = 1$ keV, 1.6T, with a launched frequency of 20 MHz and wavenumber of 9 m^{-1}.

Figure 6-18 (a) Dispersion relation for mode conversion in 50% H, 25% ^{3}He plasmas. Excited frequency is 20 MHz at a wavenumber of 10 m^{-1}, with a central magnetic field of 1.6T, central density of 5×10^{19} m^{-3} (parabolic profile), central $T_e = T_i = 1$ keV.
(b) 90% of the launched rf power is absorbed on the electrons in a single pass.

Figure 6-19 (a &b) Dispersion relation and power deposition profile for mode conversion in 10% ^{3}He, 80% H at 1.8T, 20 MHz, launched wavenumber of 6 m^{-1}, central density of 1×10^{20} m^{-3}, 1.0 keV ion and electron temperatures

Figure 6-20 (a) Cutaway view of NCSX showing the high-field side antenna. (b) Midplane cut through the NCSX vessel showing the rf antenna Faraday shields, and the plasma shape.

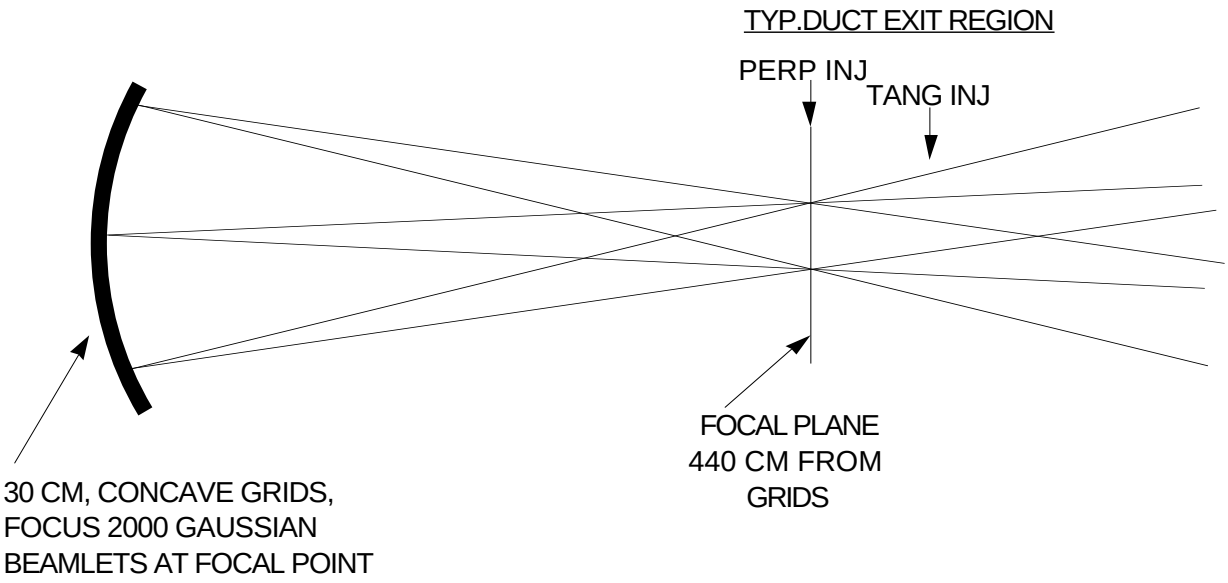

Figure 6-1. Schematic diagram of PBX-M ion source grid optics. The ion source grids are curved so as to focus 2000 Gaussian beamlets at a focal point 440 cm from the grids. Ion source optics determine the duct size and achievable aiming angles.

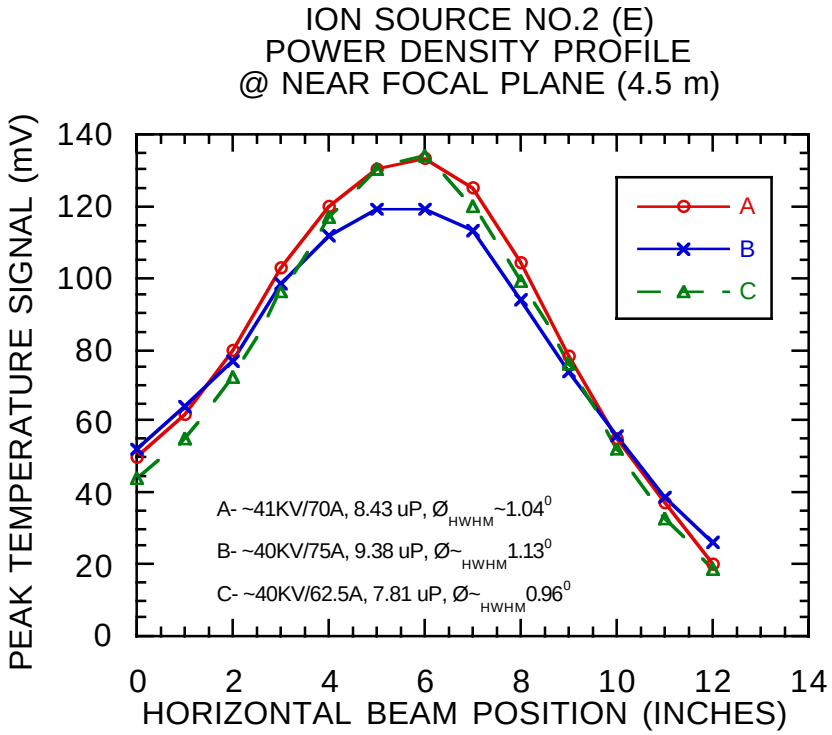

Figure 6-2. Power density profile measured at ORNL for PDX ion source No.2 (East NBI). It was found that the resultant beam trajectory at the torus target at the exit of the transition duct is not accurately determined by simple, *apriori* mechanical alignment of the ion source, and that measuring the actual beam position in the duct is important for proper beam alignment.

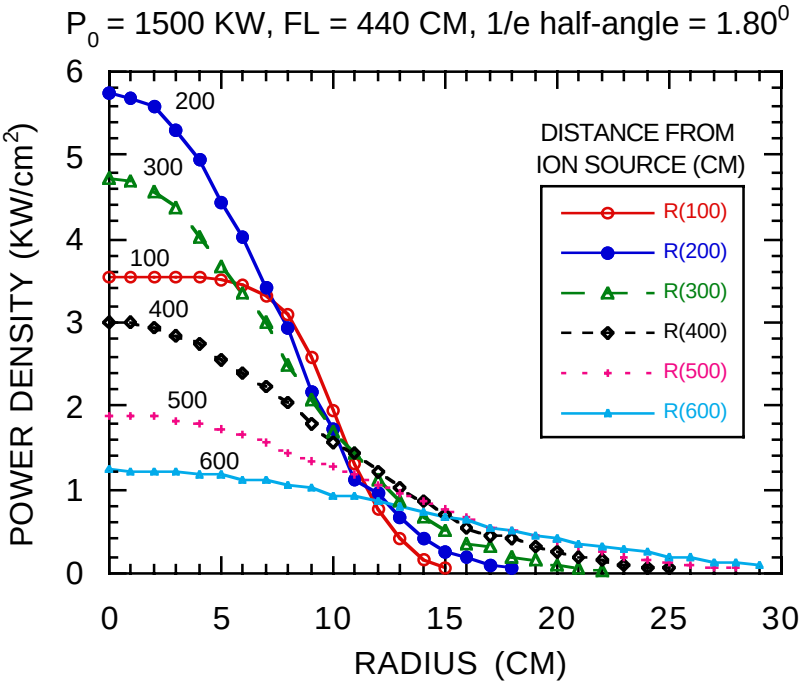

Figure 6-3. Simulated power density along beam axis. The beam port location will allow adequate duct width to avoid neutral and reionized power impingement on the duct walls.

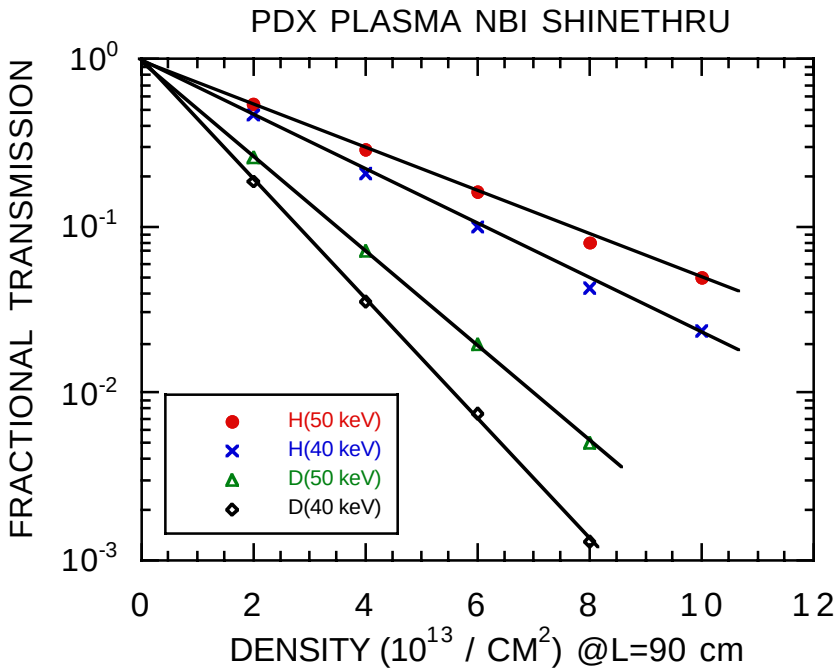

Figure 6-4. Plot of Neutral Beam power fractional transmission through a 90 cm thick PDX plasma *versus* density. This corresponds to the case of near-perpendicular injection (RTAN = 35 cm).

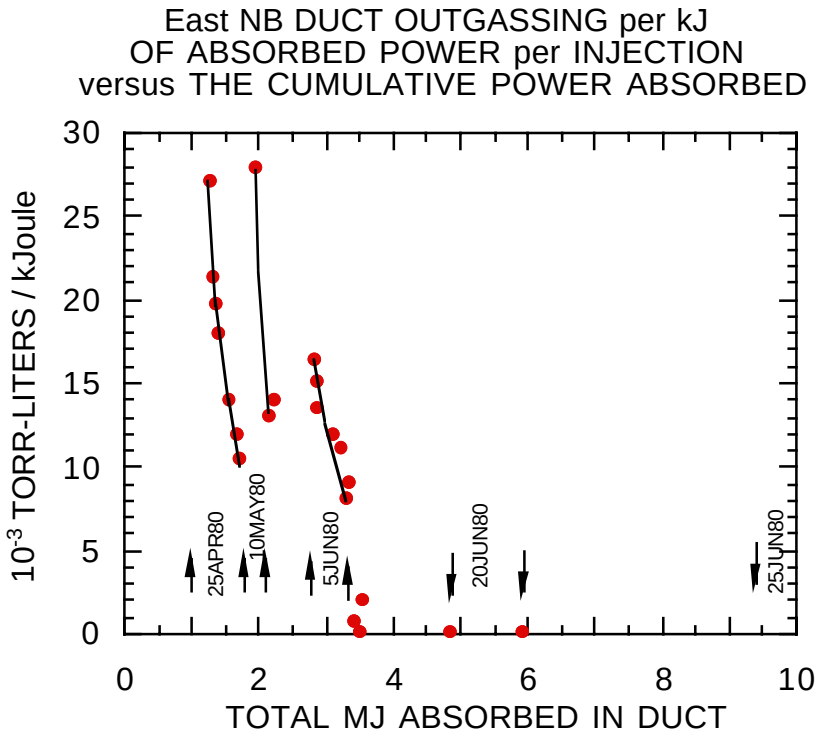

Figure 6-5. Measured PDX NBI duct outgassing during several months of operation (H.W. Kugel, et al., J. Vac. Sci. Technol., 20,(4) 1197 1982). H_2 Glow Discharge Cleaning (GDC) was used to clean the vessel immediately after pump-down from a vent. No H_2GDC or other GDC was applied thereafter. The application of HeGDC in the transition duct prior to NCSX daily operations and between discharges will reduce duct conditioning time significantly.

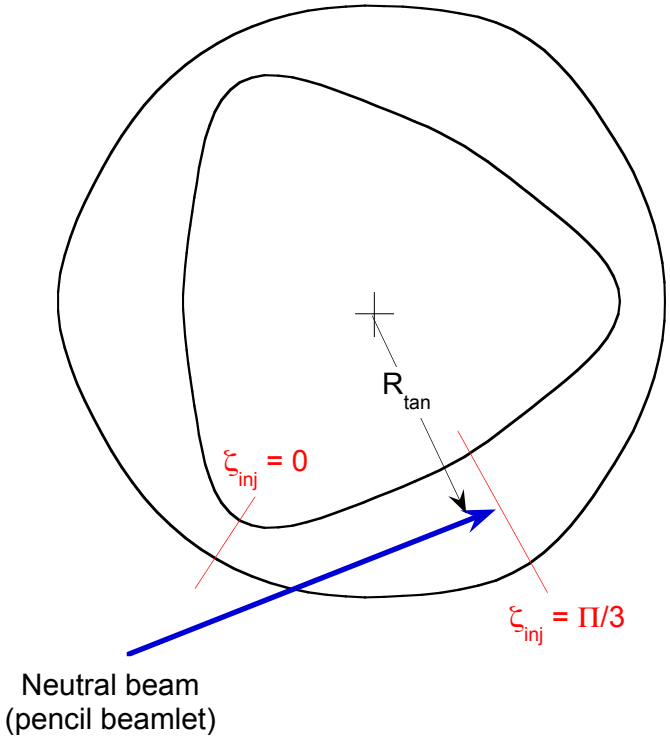

Figure 6-6. Geometry used for NCSX neutral beam calculations.

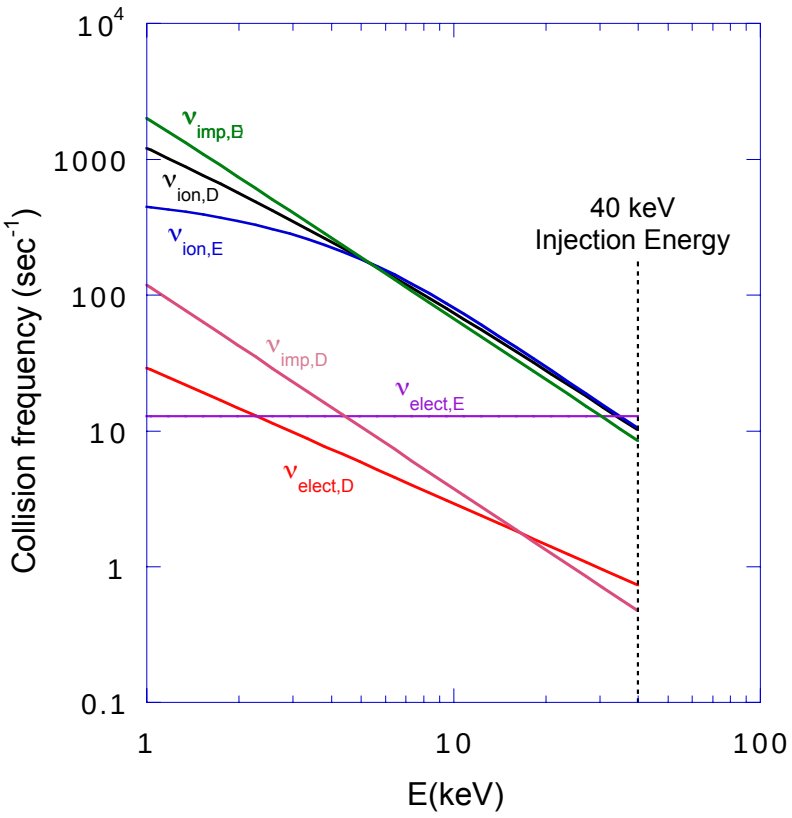

Figure 6-7(a). Collision frequencies vs. energy at r/a = 0.5 (collision frequencies with D/E subscripts denote pitch angle/energy scattering rates, respectively; ion, elect, imp subscripts denote beam collisions with plasmas ions, electrons, and impurities).

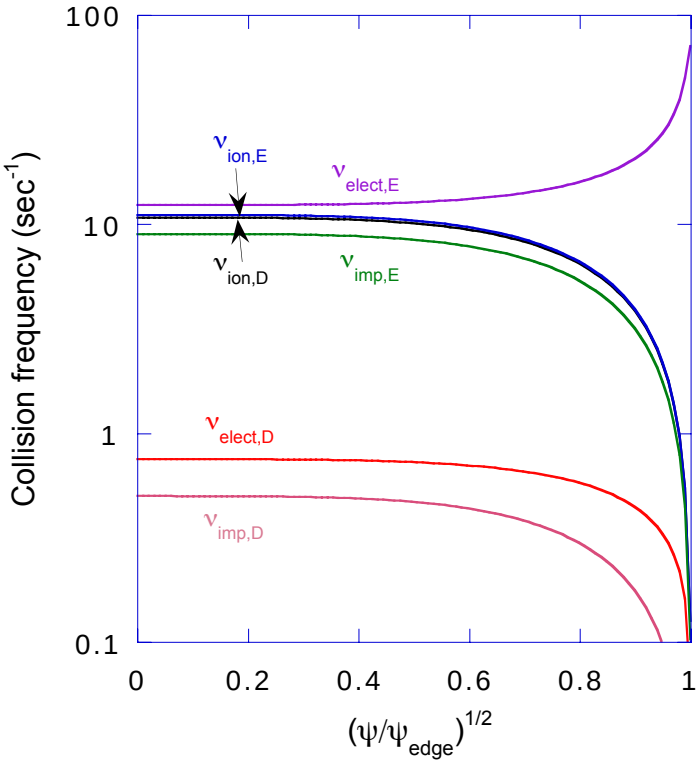

Figure 6-7(b). Collision frequencies vs. flux surface at E = 40 keV (collision frequencies with D/E subscripts denote pitch angle/energy scattering rates, respectively; ion, elect, imp subscripts denote beam collisions with plasmas ions, electrons, and impurities).

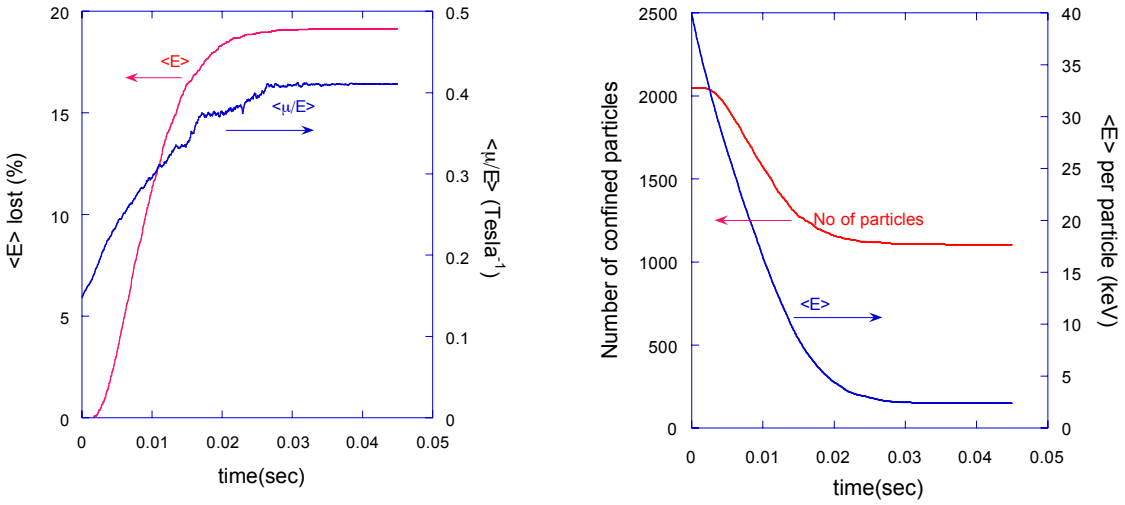

Figure 6-8(a). Typical evolution of ensemble averaged beam energy loss and <m/e>; (b). Decay in time of the number of confined beam particles and average energy per particle

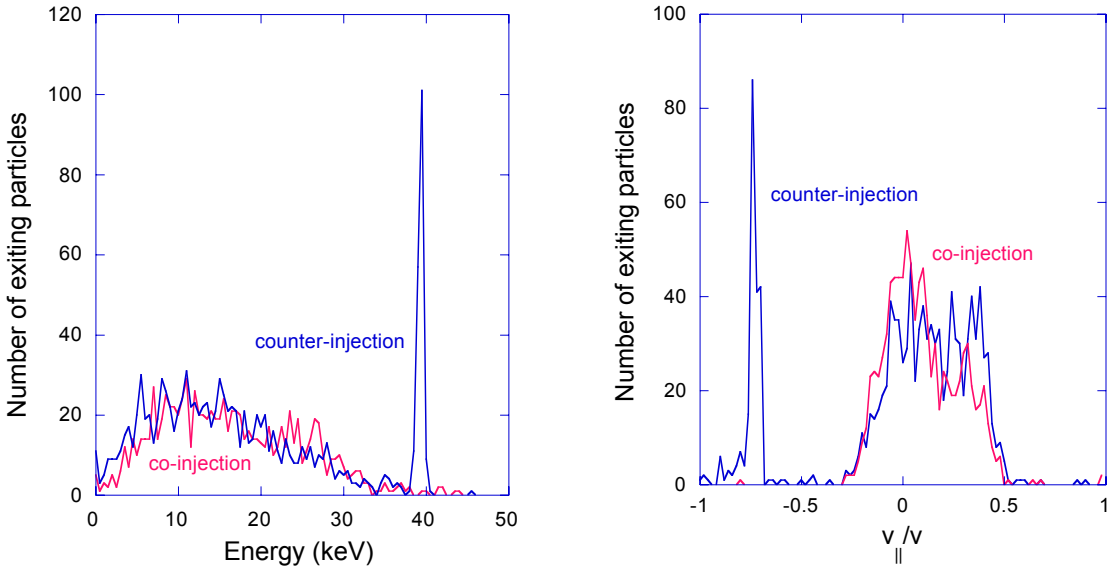

Figure 6-9(a). Energy spectrum of exiting beam particles; (b). Pitch angle spectrum of exiting beam particles.

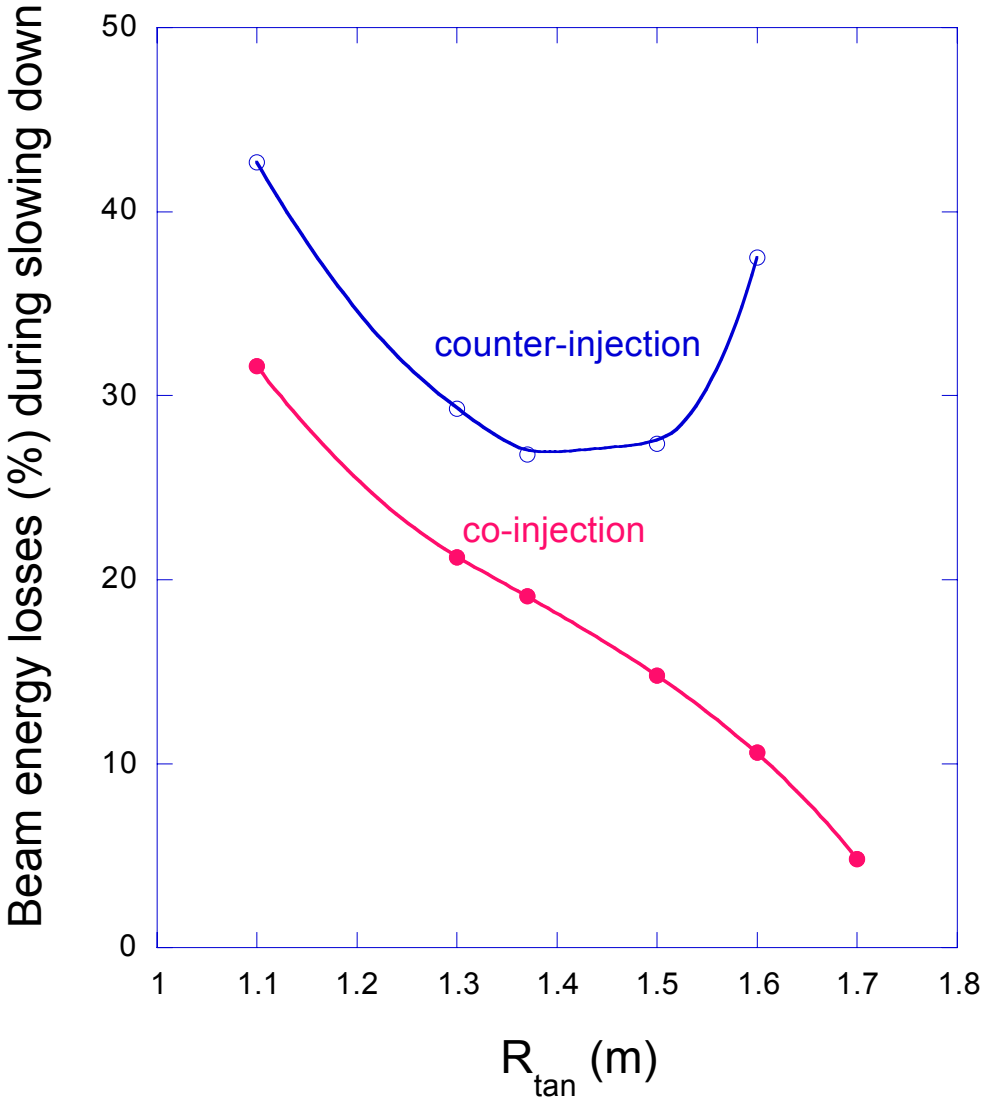

Figure 6-10 Dependence of beam losses on beam tangency radius for a version of NCSX with R_0 = 1.4 m.

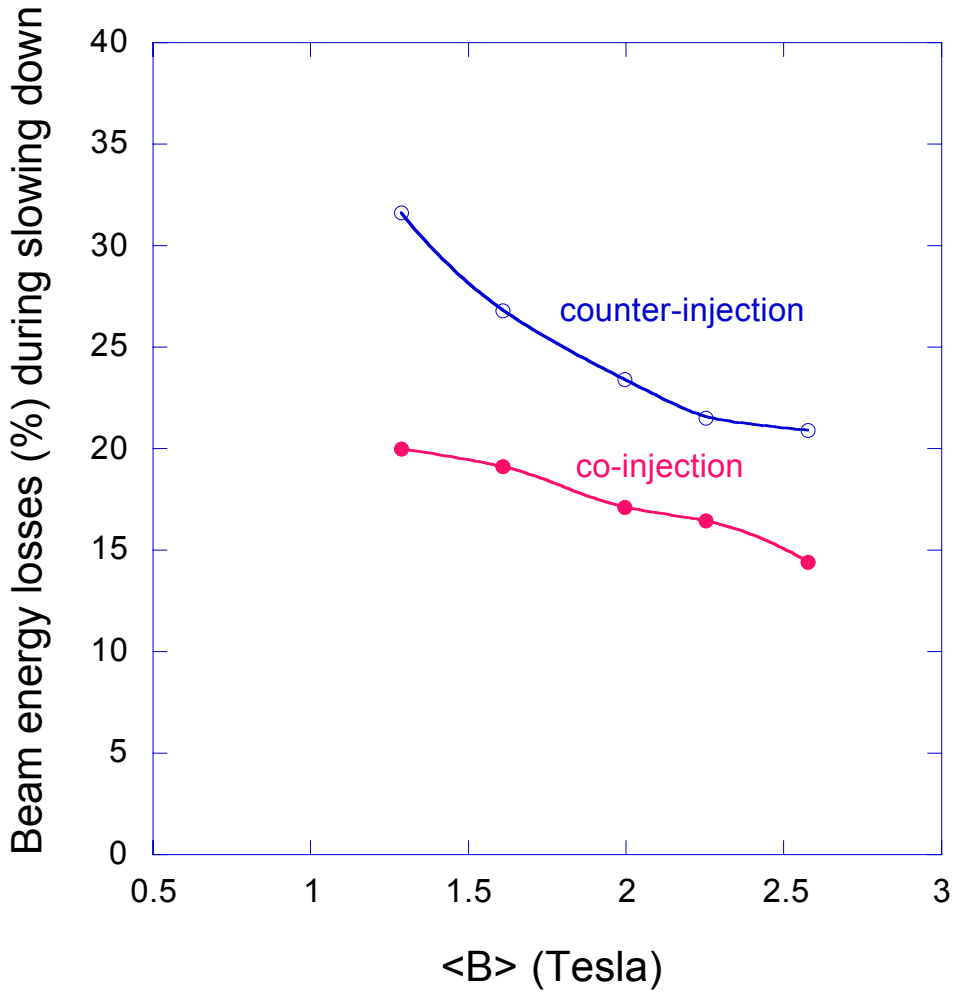

Figure 6-11. Variation of beam losses with magnetic field for 40 keV hydrogen ions for a device with R_0 = 1.4 meters.

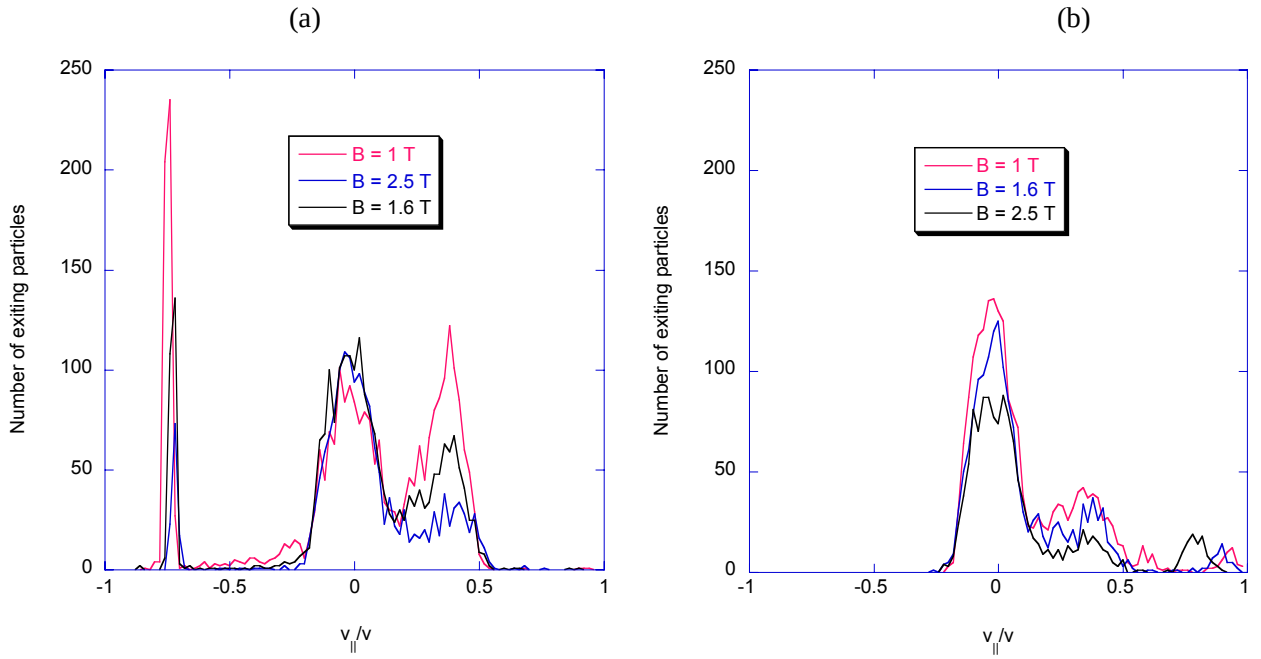

Figure 6-12. (a) Pitch angle spectrum of counter-injected losses as magnetic field is varied, and (b) Pitch angle spectrum of co-injected losses as magnetic field is varied.

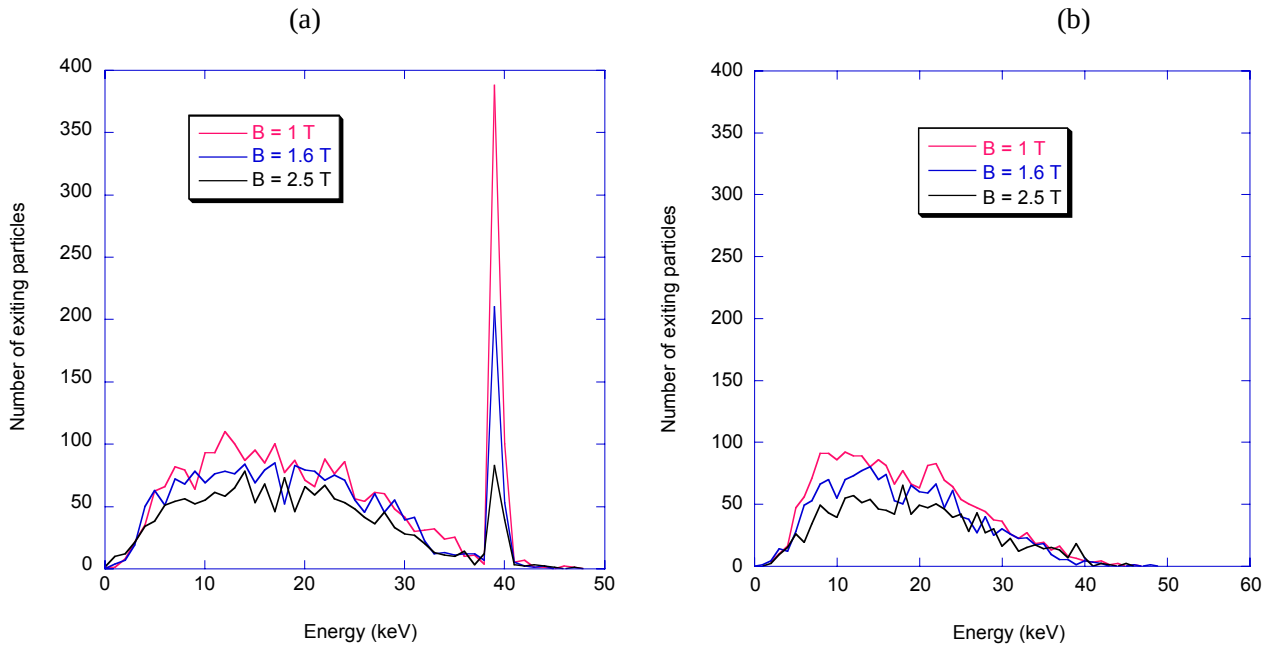

Figure 6-13. (a) Energy spectrum of counter-injected losses as magnetic field is varied, and (b) Energy spectrum of co-injected losses as magnetic field is varied.

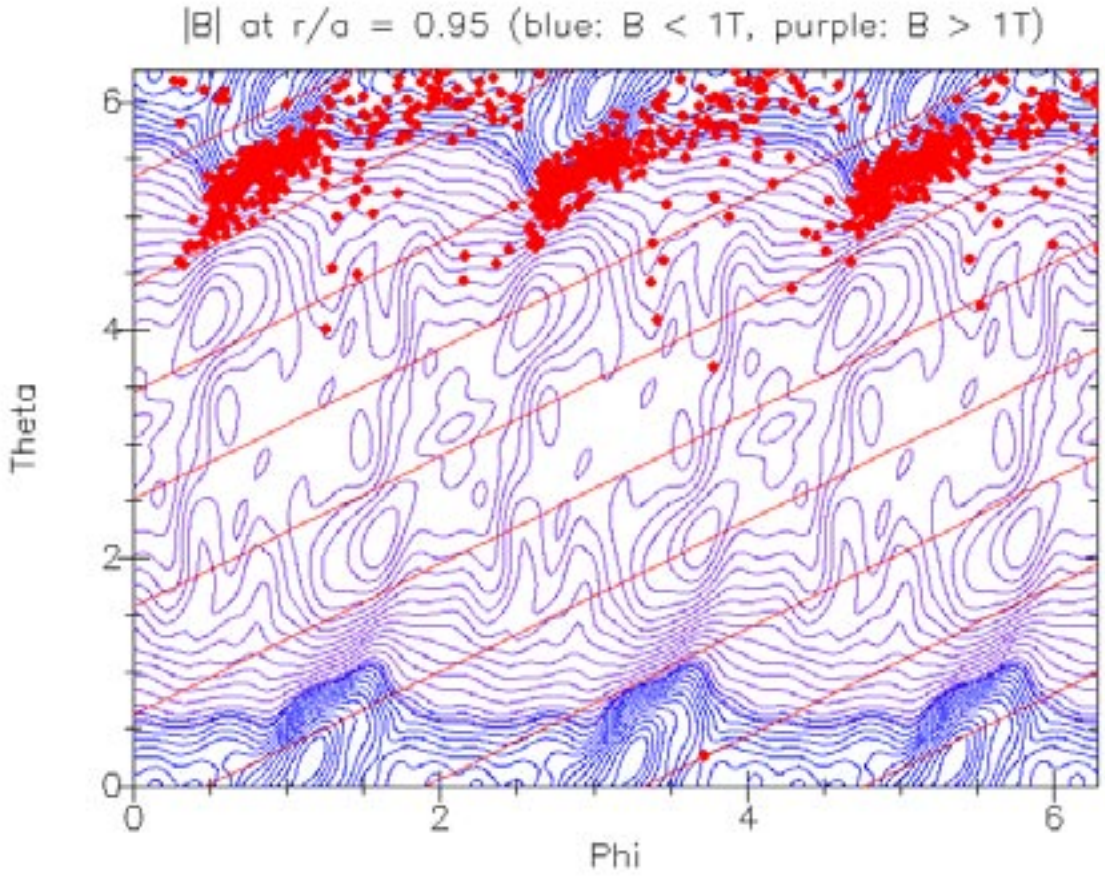

Figure 6-14. Location of co-injected beam losses (red dots) on outer surface in 2D Boozer coordinates with |B| contours and magnetic field lines (in red) shown.

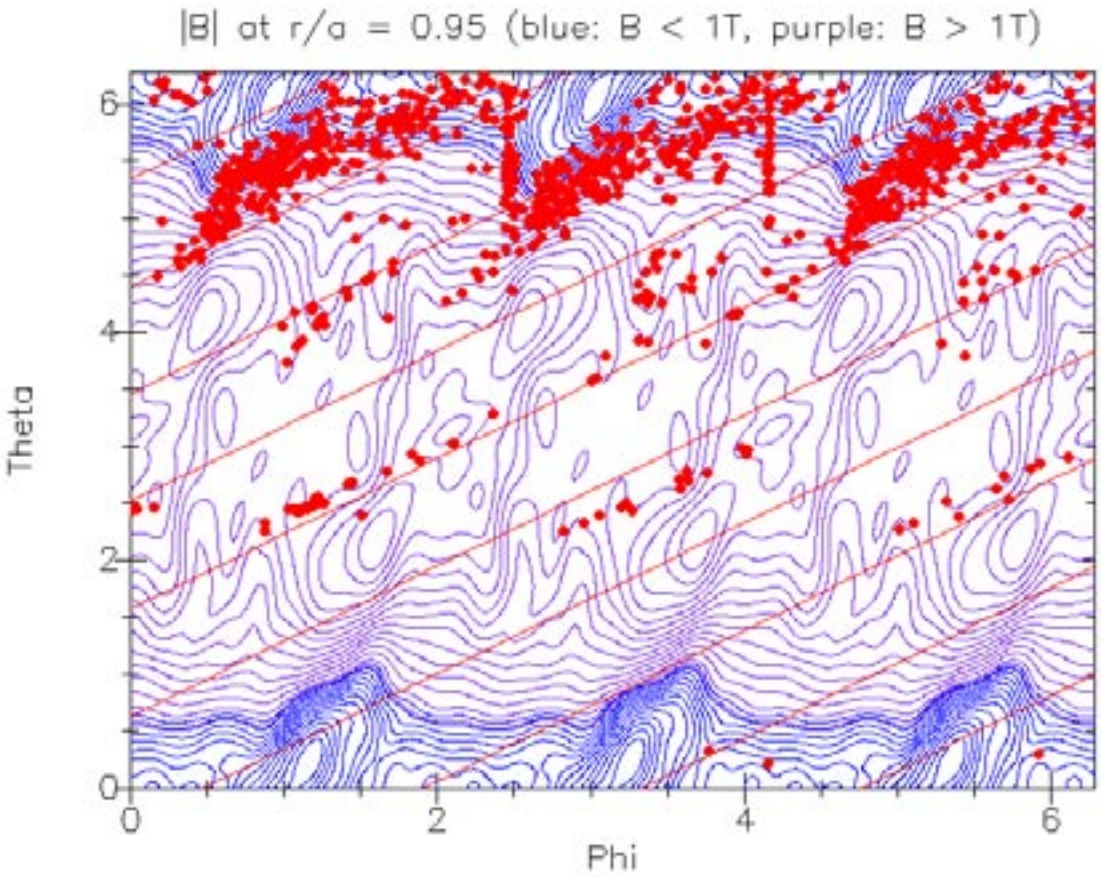

Figure 6-15. Location of counter-injected beam losses (red dots) on outer surface in 2D Boozer coordinates with |B| contours and magnetic field lines (in red) shown.

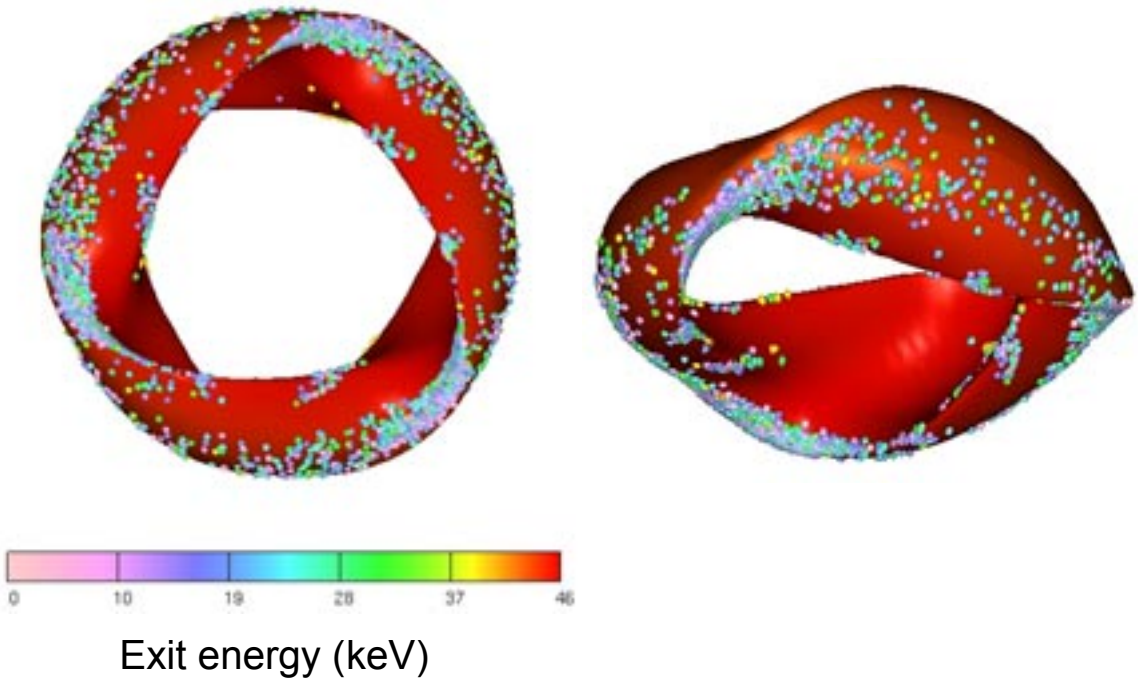

Figure 6-16. Location and energy spectrum of co- and counter-beam losses on outer surface in 3D (the outer flux surface is shown in red).

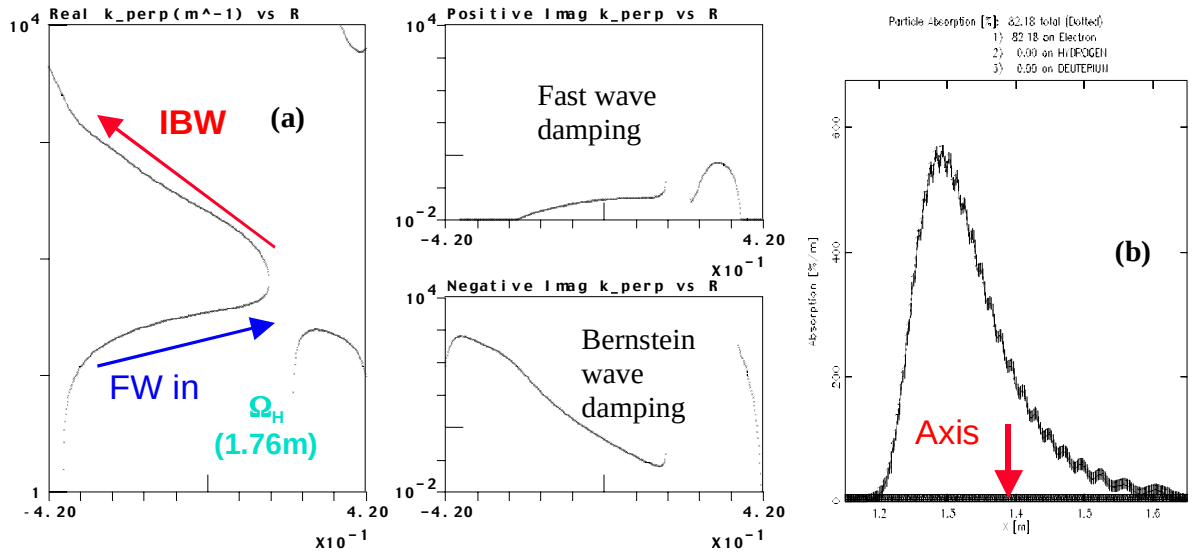

Figure 6-17. Dispersion relation for mode conversion in 10% H/90% D in NCSX (a), and power deposition profile (b). 82% of the launched power is deposited on electrons within the simulation window, with a full-width at half-max of ~15 cm. Central density for the simulation was 5×10^{19} m^{-3} (parabolic profile), central $T_e = T_i = 1$ keV, 1.6T, with a launched frequency of 20 MHz and wave number of 9 m^{-1}.

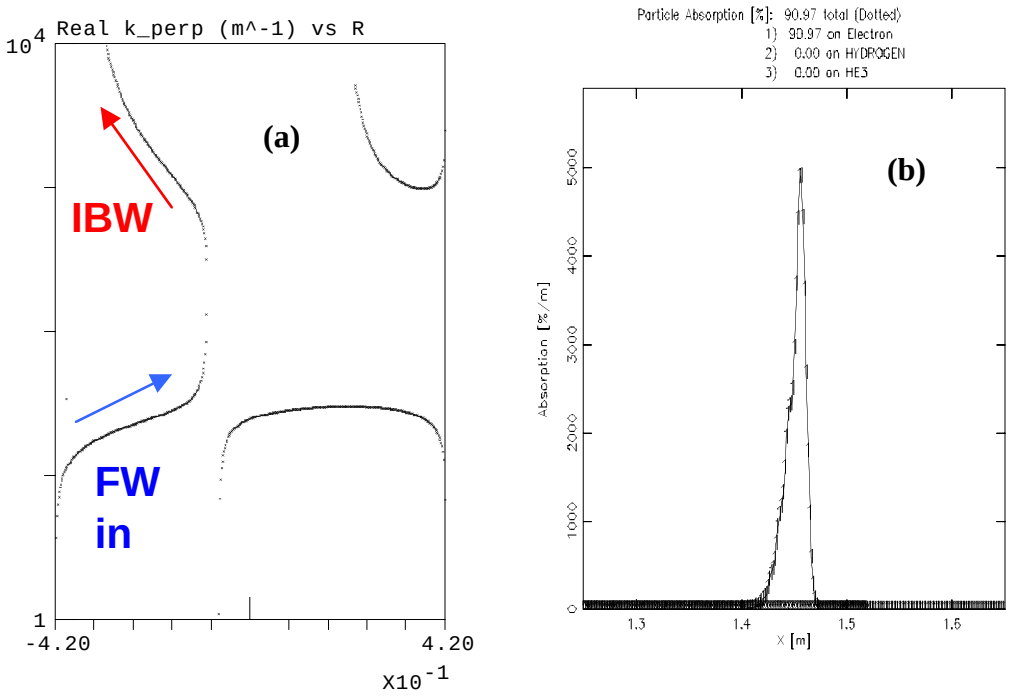

Figure 6-18 (a) Dispersion relation for mode conversion in 50% H, 25% ^{3}He plasmas. Excited frequency is 20 MHz at a wavenumber of 10 m^{-1}, with a central magnetic field of 1.6T, central density of 5×10^{19} m^{-3} (parabolic profile), central $T_e = T_i = 1$ keV.
(b) 90% of the launched rf power is absorbed on the electrons in a single pass.

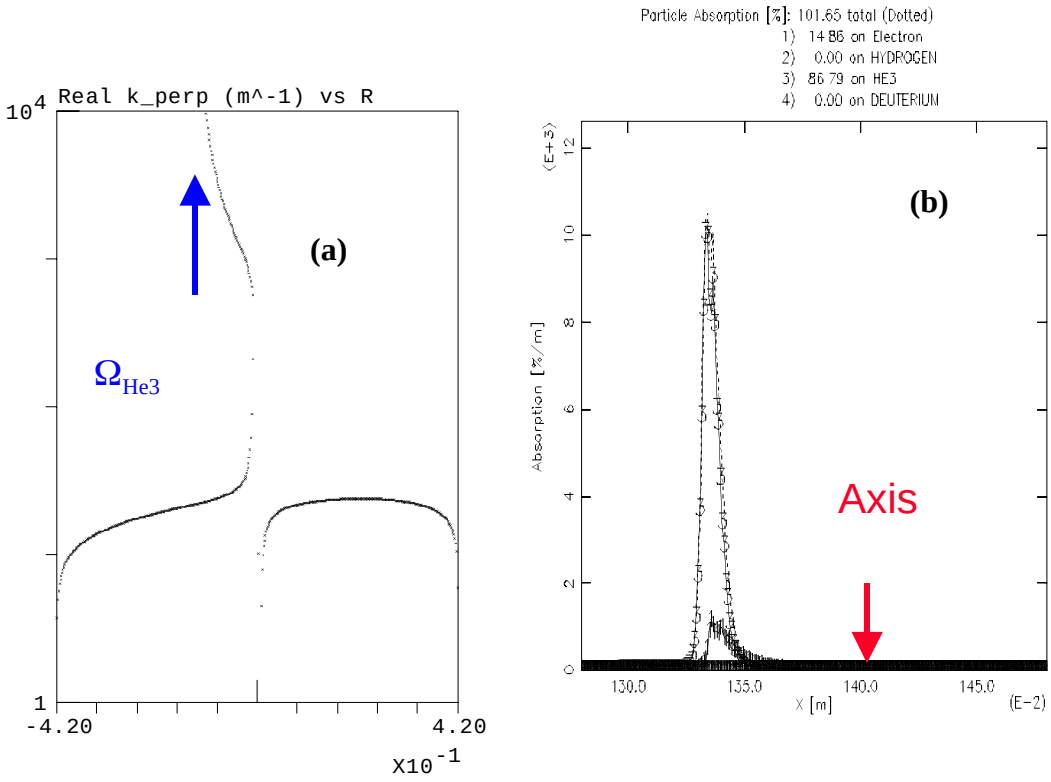

Figure 6-19 (a &b) Dispersion relation and power deposition profile for mode conversion in 10% ^{3}He, 80% H at 1.8T, 20 MHz, launched wavenumber of 6 m^{-1}, central density of 1×10^{20} m^{-3}, 1.0 keV ion and electron temperatures

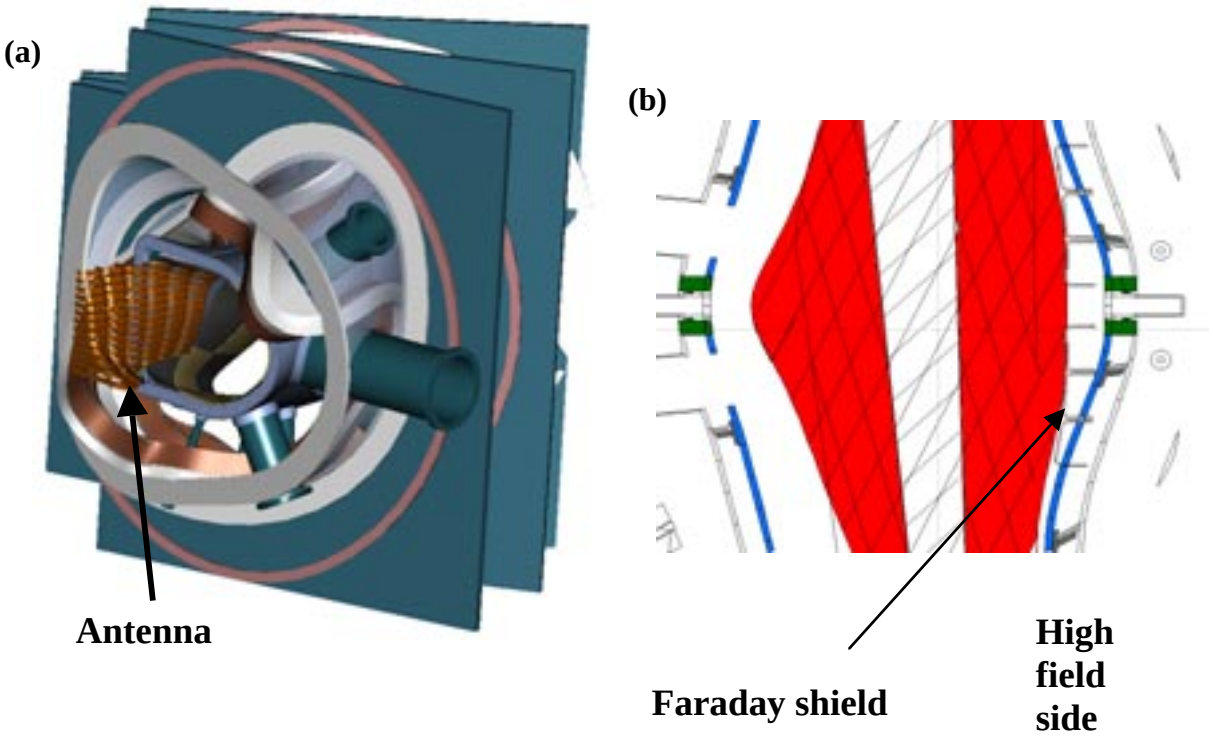

Figure 6-20 (a) Cutaway view of NCSX showing the high-field side antenna. (b) Midplane cut through the NCSX vessel showing the rf antenna Faraday shields, and the plasma shape.

External Distribution

Plasma Research Laboratory, Australian National University, Australia
Professor I.R. Jones, Flinders University, Australia
Professor João Canalle, Instituto de Fisica DEQ/IF - UERJ, Brazil
Mr. Gerson O. Ludwig, Instituto Nacional de Pesquisas, Brazil
Dr. P.H. Sakanaka, Instituto Fisica, Brazil
The Librarian, Culham Laboratory, England
Mrs. S.A. Hutchinson, JET Library, England
Professor M.N. Bussac, Ecole Polytechnique, France
Librarian, Max-Planck-Institut für Plasmaphysik, Germany
Jolan Moldvai, Reports Library, MTA KFKI-ATKI, Hungary
Dr. P. Kaw, Institute for Plasma Research, India
Ms. P.J. Pathak, Librarian, Insitute for Plasma Research, India
Ms. Clelia De Palo, Associazione EURATOM-ENEA, Italy
Dr. G. Grosso, Instituto di Fisica del Plasma, Italy
Librarian, Naka Fusion Research Establishment, JAERI, Japan
Library, Plasma Physics Laboratory, Kyoto University, Japan
Research Information Center, National Institute for Fusion Science, Japan
Dr. O. Mitarai, Kyushu Tokai University, Japan
Dr. Jiangang Li, Institute of Plasma Physics, Chinese Academy of Sciences, People's Republic of China
Professor Yuping Huo, School of Physical Science and Technology, People's Republic of China
Library, Academia Sinica, Institute of Plasma Physics, People's Republic of China
Librarian, Institute of Physics, Chinese Academy of Sciences, People's Republic of China
Dr. S. Mirnov, TRINITI, Troitsk, Russian Federation, Russia
Dr. V.S. Strelkov, Kurchatov Institute, Russian Federation, Russia
Professor Peter Lukac, Katedra Fyziky Plazmy MFF UK, Mlynska dolina F-2, Komenskeho Univerzita, SK-842 15 Bratislava, Slovakia
Dr. G.S. Lee, Korea Basic Science Institute, South Korea
Institute for Plasma Research, University of Maryland, USA
Librarian, Fusion Energy Division, Oak Ridge National Laboratory, USA
Librarian, Institute of Fusion Studies, University of Texas, USA
Librarian, Magnetic Fusion Program, Lawrence Livermore National Laboratory, USA
Library, General Atomics, USA
Plasma Physics Group, Fusion Energy Research Program, University of California at San Diego, USA
Plasma Physics Library, Columbia University, USA
Alkesh Punjabi, Center for Fusion Research and Training, Hampton University, USA
Dr. W.M. Stacey, Fusion Research Center, Georgia Institute of Technology, USA
Dr. John Willis, U.S. Department of Energy, Office of Fusion Energy Sciences, USA
Mr. Paul H. Wright, Indianapolis, Indiana, USA

The Princeton Plasma Physics Laboratory is operated
by Princeton University under contract
with the U.S. Department of Energy.

Information Services
Princeton Plasma Physics Laboratory
P.O. Box 451
Princeton, NJ 08543

Phone: 609-243-2750
Fax: 609-243-2751
e-mail: pppl_info@pppl.gov
Internet Address: http://www.pppl.gov